A Simple Doublet Lens Design for mid-IR

2 Imaging

3 CLAIRE E. NELMARK AND ARNALDO L. SERRANO*

emerging and simple means for enhancing spatial resolution.

- 4 Department of Chemistry and Biochemistry, University of Notre Dame, Notre Dame, IN 46556, USA
- 5 *arnaldo.serrano@nd.edu
- **Abstract:** Wide-field mid-IR hyperspectral imaging offers a promising approach for studying heterogeneous chemical systems due to its ability to independently characterize the molecular properties of different regions of a sample. However, applications of wide-field mid-IR microscopy are limited to spatial resolutions no better than ~1 µm. While methods exist to overcome the classical diffraction limit of $\sim \lambda/2$, chromatic aberration from transmissive imaging reduces the achievable resolution. Here we describe the design and implementation of a simple mid-IR achromatic lens combination that we believe will aid in the development of resolution enhanced wide-field mid-IR hyperspectral optical and chemical absorption imaging. We also examine the use of this doublet lens to image through polystyrene microspheres, an

1. Introduction

Infrared (IR) spectroscopy, and its ultrafast nonlinear variants, is a powerful technique useful for studying a wide range of chemical systems, materials [1–3], and phase separating systems [4,5] over a variety of timescales, [6] and has potential for biological diagnostics. [7,8] It provides extensive molecular information with a minimal amount of sample, and can be implemented in a nondestructive manner with the potential to be done in a label-free fashion. By coupling chemically sensitive information with microscopic imaging, mid-IR hyperspectral imaging collects molecular information with spatial resolution, providing an image with chemical contrast. [9,10] This is especially important in spatially heterogenous samples, where a sample can have a diverse chemical or molecular make up and it can be impossible to see how this varies using other conventional imaging modalities. [11] However, a major drawback of IR spectroscopy when studying micro-heterogeneous samples is its relatively low spatial resolution. [12]

While mid-IR imaging has been developed and used by numerous labs over decades, [13–25] due to the relatively long wavelengths of mid-IR light (\sim 3-8 µm or \sim 1250-3300 cm⁻¹) used in ultrafast mid-IR imaging, the classical diffraction limit makes it impossible to resolve smaller features such as organelles in a cell, [26] or microscopic liquid droplets. [27–29] Additionally, when a broadband light source is used for spectroscopy, chromatic optical aberrations may further limit the achievable spatial resolution. [30] Since chromatic aberration leads to reduced spatial resolution, it needs to be corrected in order to achieve diffraction-limited resolutions. Chromatic aberration is an optical aberration specific to systems utilizing a polychromatic light source, such as an ultrashort pulse of light in nonlinear optics, that arises from the wavelength dependence of the refractive index of transmissive optics. This results in the focal length of the lens being wavelength dependent, making it impossible to bring all the light from a source into focus simultaneously. [31]

Chromatic aberration needs to be addressed in even the most sophisticated transmissive optical imaging systems, regardless of the wavelength range. However, it is particularly problematic for coherent imaging in the mid-IR wavelength regime, where

commercial solutions to this problem are not widely available. With so many potentially transformative applications for mid-IR imaging, particularly in the biomedical field, there is significant interest in the development of mid-IR optical systems that can image with sub-diffraction limited resolution. [32,33] However, imaging techniques requiring a broadband light source, which is necessary for many spectroscopic applications, will suffer from reduced spatial resolution until the chromatic aberration is mitigated. While techniques to reduce chromatic aberration have been developed for visible light and include a variety of lens designs such as superchromats [34–36], hybrid lenses [37,38], metasurfaces [39,40], adaptive optics [41,42], as well as post-processing algorithms [43–46], many of these methods are expensive, time consuming, or under-developed for the mid-IR.

ATR-FTIR is a common technique touted for its ease of use and is technically capable of sub-diffraction limited resolution, however, this is only true for the sample nearest the ATR crystal. This technique is best for probing surface properties of samples, and can typically reach no farther than 5 µm into the sample, thus limiting the range of samples to be studied with it. [47,48] Reflective objectives, such as the Schwarzchild objective, are another common commercially available solution because they are intrinsically achromatic. However, these objectives have been shown previously to limit resolution capabilities for coherent imaging applications, especially near the resolution limit, due to the central obscuration of the entrance pupil caused by their secondary mirror. [13,49,50] Similarly, parabolic mirrors are inherently achromatic, and have been shown previously to also have the benefit of avoiding the central obscuration that is innate to the reflective objectives when used off-axis. [51] However, they introduce more aberration to a system when using it off-axis. Because of this, they are not favored in laser-scanning applications. [36] With an end-goal of sub-diffraction limited ultrafast imaging in mind, which requires a coherent light source, we chose to focus on the possible refractive lens options.

Besides the reflective options mentioned above, refractive solutions have been demonstrated as well. Kazarian and coworkers utilized FTIR to exhibit the ability of semi-hemispherical lenses placed on the sample to diminish chromatic aberrations. [25,52,53] Hanninen and Potma produced a promising broadband commercially constructed achromatic doublet lens that spans the visible range up to ~4.5 μ m. [36] While these are encouraging options for mid-IR techniques, they can be cost- and time- prohibitive as they are custom optics, and may require a custom optical mount. [54] Here we take a similar approach and present a simple doublet lens optimized for the 4-6 μ m (~1665-2500 cm⁻¹) wavelength region for future use in ultrafast mid-IR imaging, assembled in-lab with off-the-shelf components. This wavelength range was chosen with future ultrafast hyperspectral imaging applications studies in mind, which primarily consist of collecting information within the amide-I and nitrile region of the IR spectrum. While our design only partially corrects for the chromatic aberration present in our system, it is achievable at a fraction of the cost and time required of a fully custom solution.

Additionally, we show early work combining this doublet lens with another relatively simple technique for resolution enhancement that has been demonstrated previously. Imaging through high-index dielectric microspheres placed near to or in direct contact with the object of interest in transmission microscopy has been shown to achieve sub-diffraction resolution with visible light, [55–58], resolution enhancement when done with mid-IR light, [59] as well as effectively increase the observed magnification of the image in both cases. It is commonly believed that the reason for this resolution enhancement is related to the ability of the microspheres to focus light into photonic nanojets that have intense and narrow, sub-diffraction beam waists owing to near field effects [60,61]. Thus, coupling both the dielectric microsphere with an achromatic doublet lens has the potential to result in even greater resolving power. In

this manuscript, we have tested this approach by quantifying the resolution of the doublet lens, as well as the combination of the doublet and microsphere, by measuring their modulation transfer functions (MTFs) using a set of uniform resolution targets. Comparing amplitudes of the MTFs for different imaging systems offers an approach for identifying any resulting enhancement.

2. Methods

An air-spaced achromatic doublet consisting of a variable CaF_2 lens and an uncoated, 1" diameter, 12.7 mm focal length ZnSe aspheric lens (Edmund Optics) was designed in OpticStudio by ZEMAX. The optimal lens geometry was found with the built-in contrast optimization function that works by maximizing the intensity of the MTF at a given spatial frequency – the spatial frequency used for the optimization was 30 cycles per mm. The combination was first optimized allowing the thickness of the lens, the air spacing between the two lenses, the air spacing from the second lens to the image plane, and the radius of curvature of both sides of the CaF_2 lens, to vary.

From here, the optimized CaF_2 lens was compared to off-the-shelf models from various manufacturers, and a meniscus lens from Thorlabs, Inc. very nearly matched the optimized parameters. The specifications for this meniscus lens were swapped out for the optimized CaF_2 lens in OpticStudio and the doublet was reoptimized allowing the space between lens and the space after the lens to the image plane to both vary. The CaF_2 meniscus lens was placed in a slotted lens tube with the ZnSe aspheric lens at approximately the optimized distance. Fine adjustments were then made with the retaining rings while optimizing the apparent contrast in the live digital microscope images. A diagram of the microscope is shown in **Fig. 1(a)**.

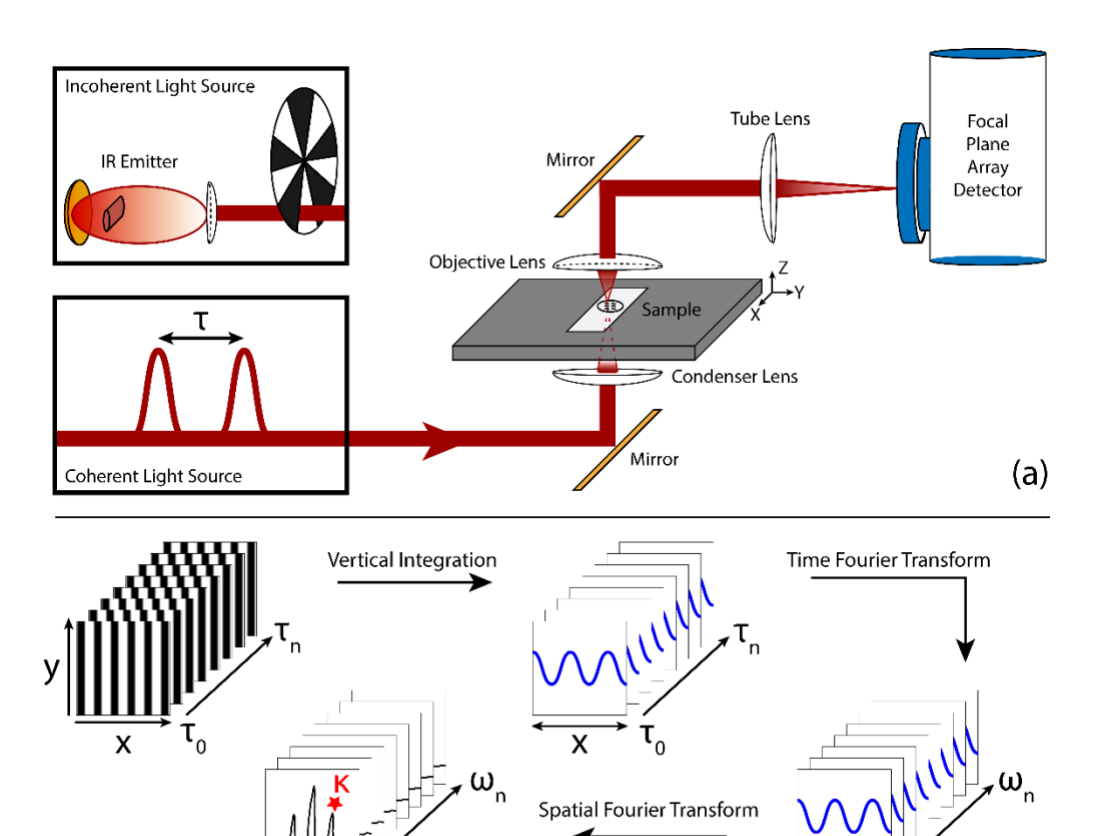


Fig. 1. (a) Diagram of the microscope setup. For coherent experiments, the light source in the black outline is a double pulse sequence generated by our AOM-based pulse shaper using broadband pulsed laser light from our femtosecond (fs) mid-IR laser system. For incoherent experiments, the setup in the top black outline was used. The objective lens was also switched between the asphere and the doublet lens, depending on the experiment. (b) Depiction of the FTIR image processing scheme. Images without NAP spectra were processed in a similar manner, but without the time Fourier transformation step.

(b)

A homebuilt wide-field mid-IR microscope was configured using the newly designed doublet lens as the objective lens, and a similar ZnSe aspheric lens (Edmund Optics) with a numerical aperture (NA) of 0.71 as the condenser lens. A CaF_2 lens with a 50 mm focal length was used as the tube lens to allow for ~50x magnification of the images. Images were collected on a 128×128 -pixel mercury cadmium telluride (MCT) focal plane array detector (Catalina, Teledyne) at the imaging plane.

A custom chrome patterned CaF_2 resolution target (II-IV Optical Systems) with Ronchi grating patterns from 50 to 500 line pairs per millimeter (lp/mm), in increments of 50, was used for imaging with both incoherent and coherent light sources. The broadband coherent light source, centered at 6 μ m with a full-width at half-maximum band width of ~150 cm⁻¹, originated from an AOM-based ultrafast mid-IR laser system described previously. [59] A 9W IR light emitter (Newport) placed in front of a 75 mm focal length gold spherical mirror and collimated with a 150 mm focal length CaF_2 lens was used as an incoherent light source. To

image through microspheres, $100 \mu m$ polystyrene (PS) microspheres (Spherotech) with a mid-IR refractive index ~1.5 [62] suspended in spectroscopic grade methanol were placed dropwise onto the set of gratings until each grating had at least one lone microsphere for imaging. Images were collected at each grating frequency, with and without a PS microsphere, using both coherent and incoherent light sources. Blank images were also collected through unobscured regions of the CaF_2 target at the same focal settings as each collected grating image, for later background subtraction.

After images were processed (i.e., background subtracted and dead pixels were replaced with the averaged value of nearest neighbors), horizontal cuts of the intensity were taken from the center of each image and vertically averaged over a number of rows, with the averaged cut being Fourier transformed to generate a spatial frequency spectrum. With a lp/mm axis the amplitude of the peak nearest the expected spatial frequency was collected. This was typically the second largest peak in the spatial frequency spectrum, shown in **Fig. 1(b)** and denoted as κ, since the center peak, corresponding to 0 lp/mm, had the largest amplitude. The intensity of the chosen peak was plotted against the actual spatial frequency of the grating to generate the experimental MTFs. The MTFs for the gratings with PS microspheres were each normalized to a 0 lp/mm point. The 0 lp/mm point was taken by collecting an image through a portion of solid chrome on the grating slide, a cut was taken through this in the same manner as the other cuts, and subtracted from the cut for 50 lp/mm. This new subtracted cut was divided by two to account for half of every line pair being covered with chrome, and Fourier transformed to collect the spatial frequency in the same way as the others.

Error bars were determined by choosing wing regions of the Fourier transform that did not include the expected peak, or any intense peaks from higher harmonics of the given spatial frequency. The root-mean-square (RMS) of the wing region was then calculated to give the error in MTF amplitude for each data point. Error was also calculated to look at the noise in the data collection process. For this, 100 shots were collected and averaged into a file. Ten of these files were collected, and individually processed following the same procedure described above. The intensity of the peaks was collected for each of these ten files, and the standard error of the mean was calculated for this data set. As this error was much smaller than that calculated from the wing region in our processing (on the order of $\sim 1.5\%$), we decided this error was negligible and thus presented the larger error from our processing.

The final set of data collected contained FTIR images taken of N-acetyl proline (NAP) on the gratings to determine the spatial resolution of chemical absorption imaging. For this, 200 mM D₂O-exchanged NAP solution was placed dropwise over the gratings. This was covered with a 50 μm greased Teflon spacer and a 0.35 mm CaF₂ window. Images were collected in a purged environment at the focus of the gratings through the NAP solution and averaged for ~10 minutes. As the blank, a sample of D₂O was prepared in the same way on a blank CaF₂ window and a spectrum was collected at the same focus as the NAP sample was collected. Data processing was done following the depiction in Fig. 1(b). During image collection, our femtosecond IR pulses were shaped into double pulse pairs with varying phase and time delays, τ. A series of images, shown first, were collected and processed with a two-frame phase cycling scheme described in [13] to produce time-domain interferograms for each pixel in the images. The data was then vertically integrated, and time Fourier transformed to generate single beam spectra for the stack of images, as shown by the next two arrows and stacks of images. The blank sample described above was processed in the same way to generate blank spectra that were used in calculating the absorbance spectra for the image stack. Finally, as illustrated by the last arrow and stack of images in Fig. 1(b), the data underwent spatial Fourier transformation to extract the spatial modulation at each grating frequency. Within these averaged FTIR spectra, the 1700 cm⁻¹ peak characteristic of NAP [63], shown in Fig. 7(a), was

baseline-corrected for each set of gratings using a linear fit, and the peak intensity was plotted against the corresponding spatial frequency of the grating. The error bars were generated in a similar fashion to the optical MTF described above.

3. Results

3.1 Designing the Lens

A doublet was chosen for its simplicity and relatively small size. For a doublet to correct for chromatic aberration between two different wavelengths, there must be a dispersion difference between these materials. Thus, the materials for a doublet are typically selected based on their location in an Abbe diagram, [64] which plots the Abbe number V vs. the refractive index n of a set of materials over a specified wavelength range. Since the Abbe number is a measure of the dispersion of a material, this number should be significantly different for the two materials. The Abbe number can be calculated with **Eq. 1**, where n_{center} is refractive index of the material at the center wavelength of the chosen range, n_{short} is at the shortest wavelength of the range, and n_{long} is at the longest wavelength in the range. [65] An Abbe diagram consisting of common mid-IR optical materials was calculated with refractive index data from Zemax OpticStudio [66] from 4-6 μ m and is shown in **Fig. 2**.

$$V = \frac{n_{center} - 1}{n_{short} - n_{long}} \tag{1}$$

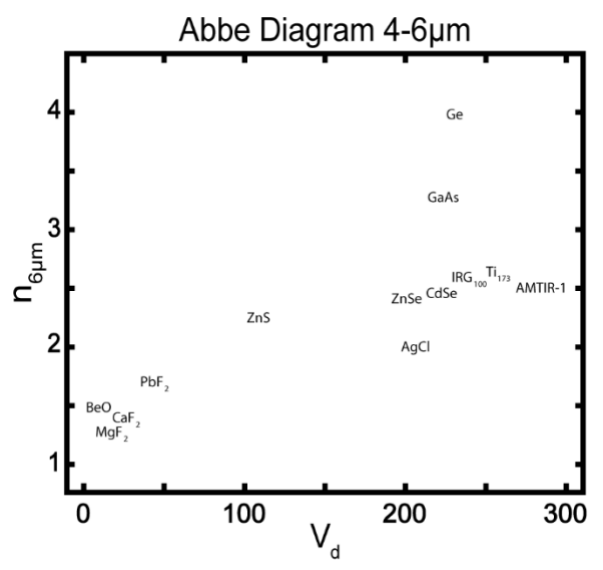


Fig. 2. Abbe Diagram from 4-6 μ m (\sim 1665-2500 cm $^{-1}$) for mid-IR transmissive materials. Data for refractive index and Abbe number from Zemax OpticStudio [66], and diagram adapted from Salv, et. al. [67]

Numerous combinations of materials on opposite ends of the Abbe Diagram were used to model the doublet lens (data not shown), but ultimately, we chose to use a ZnSe asphere as the second lens and vary the geometric parameters of the first lens. In the end, CaF₂ was chosen because it is a very common mid-IR material and had a wide separation from ZnSe in the Abbe diagram.

Optimizations were run to design a manufacturable lens that would fit within the space constraints of our microscope, allowing every aspect of the CaF₂ lens to vary except for its aperture size. Due to these manufacturing and space constraints, thickness constraints were placed on the optic to keep it between 2-15 mm, and on any air spacings (between the two lenses, and from the asphere to the imaging plane) to be between 2-50 mm, with all edge thicknesses at a minimum of 2 mm. Contrast optimization produced a CaF₂ lens with a favorable combination of MTF, spot size, and PSF with similar dimensions to a CaF₂ meniscus lens that could be purchased off the shelf from Thorlabs. **Table 1** compares the parameters of the two lenses.

Table 1. A Comparison of the two CaF₂ lenses: the theoretical lens produced by contrast optimization and the real meniscus lens from Thorlabs.

	Optimal Lens	Real Lens
Radius of Curvature – Front Side (mm)	42.007	42.0
Radius of Curvature – Back Side (mm)	21.151	20.2
Center Thickness (mm)	7.367	4.0
Edge Thickness (mm)	11.662	6.5

The parameters for the optimized CaF_2 lens were replaced with those from the commercially available meniscus lens, and the optimization process was redone, this time only allowing the distances between lenses and from the second lens to the imaging plane to vary. The resulting metrics did not change dramatically from the optimized case and were deemed suitable for our purposes.

is shown in **Fig. 3**. These results are for contrast optimization at 30 cy/mm for 4-6 μ m in OpticStudio. The spot size of the doublet was narrowed to an RMS radius of 12.404 μ m, which is a huge improvement over that of the asphere at 49.323 μ m. Finally, and most importantly for experimental comparisons, the normalized MTFs show that the doublet has increased amplitude at higher spatial frequencies when compared to that of the asphere. This correlates to improved image resolution.

Comparison of the final doublet design with the commercial lens versus the asphere

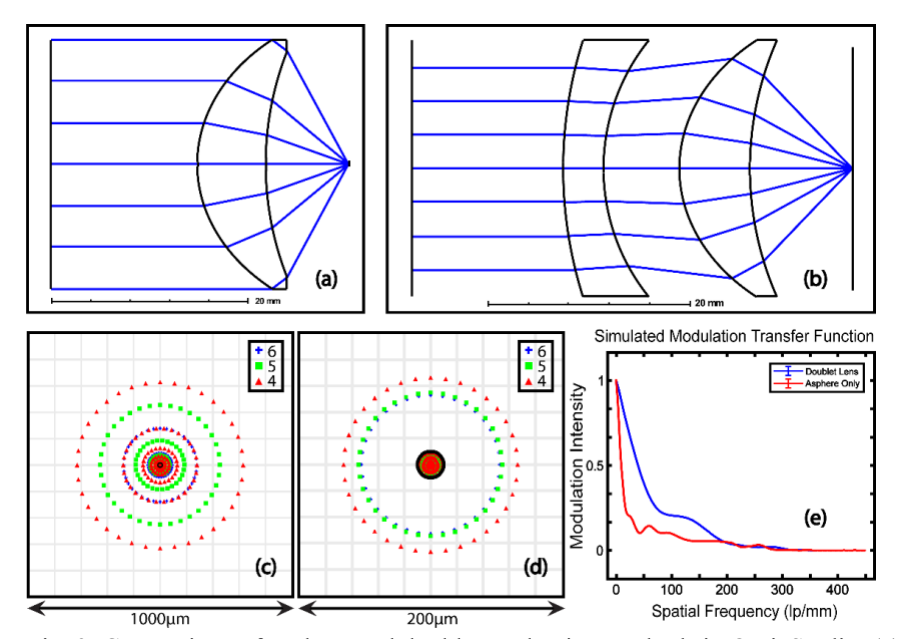


Fig. 3. Comparison of asphere and doublet evaluation methods in OpticStudio. (a) Asphere layout. (b) Doublet layout. (c) Spot size diagram for 4, 5 and 6 μ m light through the asphere. (d) Spot size diagram for 4, 5 and 6 μ m light through the doublet. The black ring in the middle is the Airy disk size. The black rings in the middle of the spots mark the Airy radii for the given clear aperture of the imaging system. (e) Normalized MTFs for the asphere (red) and doublet (blue). The doublet shows a much higher intensity at lower spatial frequencies, which would result in clearer images.

3.2 Evaluation of the Lens

Both lenses – the CaF₂ meniscus lens (**Table 1**) and the ZnSe asphere – were housed in a slotted lens tube and held in place with adjustable retaining rings. Adjustments were made to the lens spacing, and the microscope was reconfigured with the new doublet prior to collecting and processing images as described in the Methods section. Following this, horizontal cuts of the intensity were taken through the center of the image to avoid consistent imaging artifacts from the edges of the detector array, which can be exemplified by noise in the top right corner of each image. These cuts were vertically averaged over the region shown by the white box in each image. Selected images and their cuts are shown in **Fig. 4**.

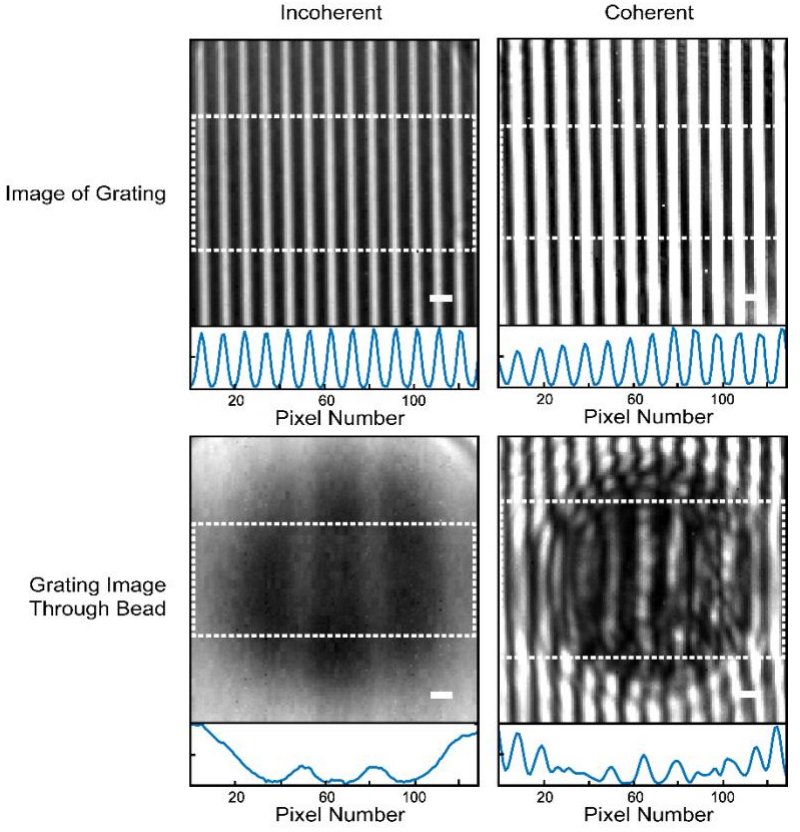


Fig. 4. Comparison of incoherent and coherent microscope images for the 100 line-pairs per millimeter (lp/mm) grating. The top row shows images of just the grating, while the bottom row of images is through 100 μ m PS microspheres. The blue trace below each image is the averaged cut taken from the box within the dotted white line on each image. The white scalebar in each image represents 12 μ m.

The averaged cuts were each Fourier transformed to pick out the amplitude of the peak nearest the expected spatial frequencies. When analyzing images taken through microspheres, averaged cuts to be Fourier transformed were only taken from the section of the image containing the microsphere to look for possible resolution enhancement, rather than including sections of plain grating for analysis. The intensity of the chosen peak was plotted against the actual spatial frequency of the grating to generate the experimental MTFs. Calculation of the error bars is described previously in Methods. **Fig. 5** shows a comparison of the experimental MTFs produced by the doublet versus by the asphere. MTFs resulting from the coherent light case are shown in **(a)** and the MTFs from the incoherent light are shown in **(b)**. All MTFs were normalized to the 50 line-pairs per millimeter (lp/mm) point.

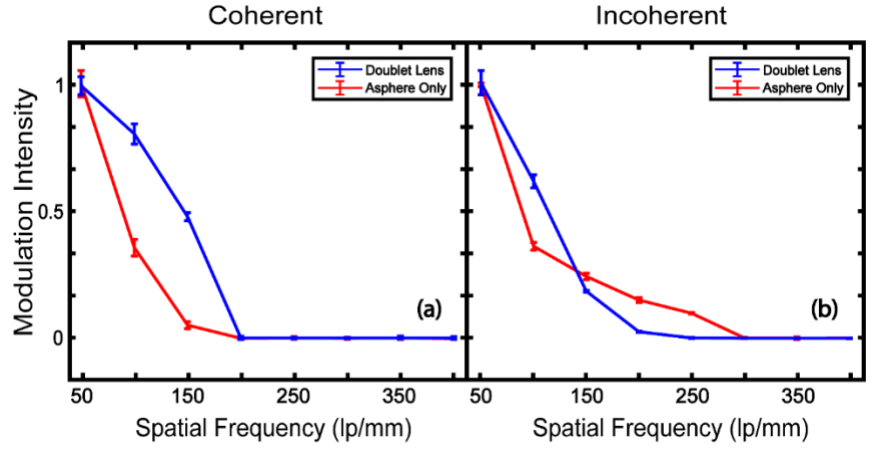


Fig. 5. Normalized MTFs for asphere (red) and doublet (blue) collected with (a) coherent light centered at 6 μm and (b) incoherent mid-IR light. All MTFs were normalized to the 50 lp/mm point.

For the coherent light source, the doublet shows a clear increase in modulation intensity over the asphere at low spatial frequencies, corresponding to resolution enhancement. However, both the asphere and doublet cutoff at the same spatial frequency of 200 lp/mm, which corresponds to the coherent cutoff for 6 μ m at ~166 lp/mm. This means that when used with a coherent mid-IR light source, the doublet produces images with more distinguishable features than the asphere but is not able to show any features smaller than the asphere is capable. The incoherent light source yields different results. The doublet initially shows some improvement in modulation intensity when imaging at lower spatial frequencies but performs worse than the asphere at spatial frequencies starting at 100 lp/mm and higher. The asphere was capable of imaging smaller features overall than the doublet, as well.

Next, images were taken through PS microspheres placed on the gratings. As discussed earlier, the addition of a PS microsphere has been shown to increase resolution. Thus, the MTFs presented in **Fig. 6** were calculated for the images through a 100 μ m PS microsphere on each grating. However, these MTFs appear to not follow the expected behavior. The lack of spatial resolution enhancement with the addition of the PS beads is discussed later.

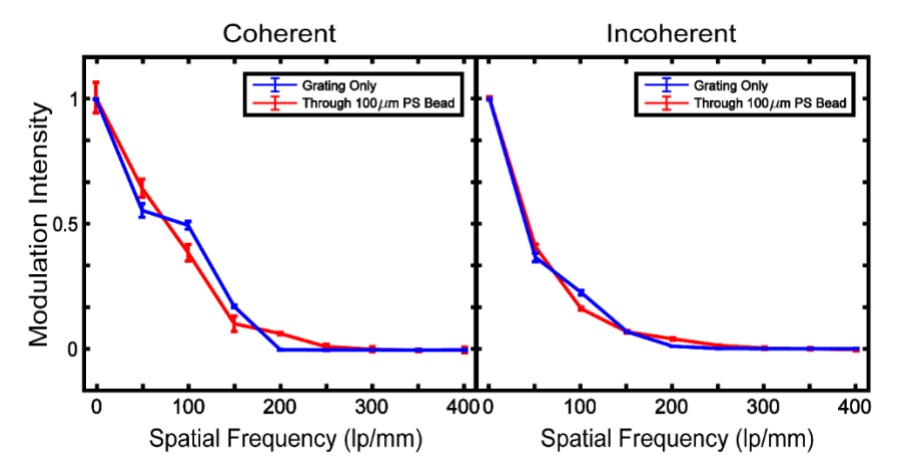


Fig. 6. MTFs taken with the doublet through 100 μm PS microspheres compared to images collected of just the grating for (a) coherent light centered at 6 μm and (b) incoherent mid-IR light. In both graphs, the blue curve is the grating only, and the red curve represents imaging through the PS microspheres.

Finally, FTIR microscope images were collected in order to assess the spatial resolution in FTIR absorption imaging. For this set of data, images were collected of the gratings through NAP solution superimposed on the gratings. Since the gratings were more difficult to see through the NAP than on the clean resolution targets, a smaller selection of grating spacings was collected. A normalized spectrum of the NAP peak used to generate the MTF is shown in Fig. 7(a). The resulting MTF can be seen in Fig. 7 (red), with the optical MTF collected from the gratings earlier (blue) for comparison.



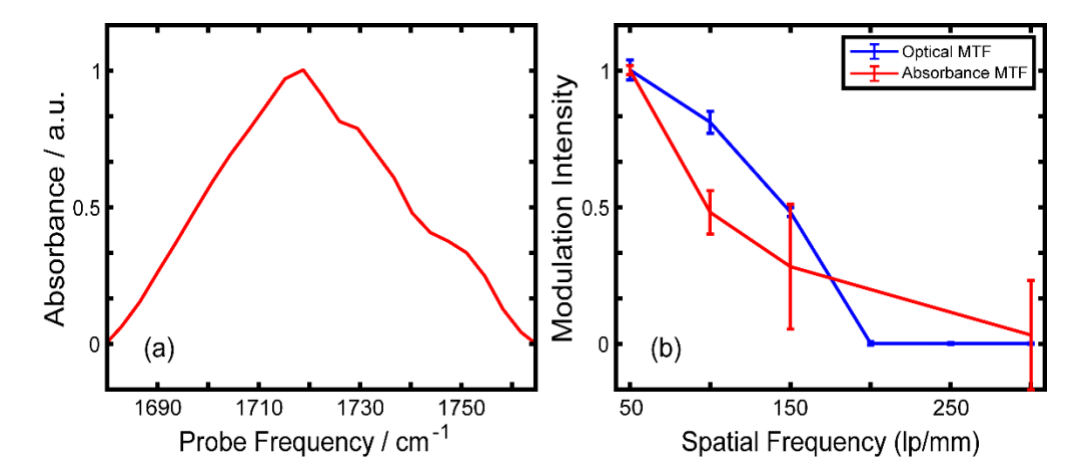


Fig. 7. (a) Normalized FTIR spectra of NAP resulting from the absorbance processing described above. The absorbance peak was collected and baselined for each of the selected grating spacings with the intensity used as the modulation intensities in the absorbance MTFs in (b). (b) Normalized MTFs collected with the doublet lens to compare the spatial resolution through optical intensity (blue) and absorbance measurements (red). The optical MTF (blue) is the same as the blue MTF plotted in **Fig. 6(a)** collected through the plain grating. The absorbance MTF (red) was collected with the absorbance spectrum of NAP on each of the grating spacings.

4. Discussion

As shown in **Fig. 5**, the resolution is improved when imaging with the doublet with coherent light when compared to previous results from the asphere. This is due, in part, to a reduction in coherent ringing artifacts that has previously been reported in coherent mid-IR imaging. [59,68,69] Additionally, when normalizing the grating MTF with coherent light to 0 lp/mm, **Fig. 6**, the experimental doublet produced an MTF that follows a similar shape as the simulated doublet MTF produced in OpticStudio shown in **Fig. 3**. Imaging done with incoherent light, however, did not produce the same results. Instead, the doublet only appears to slightly increase the resolution at 50 and 100 lp/mm, before being outperformed by the asphere. One reason for the incoherent light not performing as well as the coherent light in terms of the MTF might be the fact that the doublet was optimized for 4-6 µm (~1665-2500 cm

 1) light in OpticStudio. The incoherent light source spans from approximately 1-25 μ m (\sim 400-10,000 cm $^{-1}$), which is much broader light than the doublet is optimized for, making lower resolution likely. However, in the future, this can be mitigated with a bandpass filter that only allows through a similar wavelength range as that of the coherent light source.

The addition of the 100 µm PS microspheres shows almost no resolution enhancement as compared to images of the bare grating. This is unexpected given our previous work, in which the microspheres enabled us to resolve gratings at much higher spatial frequencies than calculated frequency cutoffs would predict. [59] One possibility for this could be due to an effect caused by the addition of the CaF₂ lens. We hypothesize that because PS has a mid-IR refractive index similar to CaF₂, [53] the ZnSe asphere and PS previously acted to offset each other, similar to a crude doublet lens. The addition of the CaF₂ may have disrupted this offset, causing the benefits of the microspheres to all but disappear. This effect seems to be worse in the incoherent case, in support of the idea that the incoherent light source is too broad for the doublet as currently designed and arranged. In the MTF generated with FTIR absorption imaging of NAP, we see somewhat similar spatial resolution capabilities as with the intensity MTF, though it does drop off more gradually and ends around the same grating spacing.

While the doublet lens designed here is meant to correct for chromatic aberration in IR imaging systems using broadband sources, an alternative approach would be to utilize a tunable source such as a quantum cascade laser, as is used in discrete frequency IR imaging systems. In such cases, chromatic aberrations could be mitigated by simply adjusting the focal plane at every frequency, without the need of the achromat.

5. Conclusion

Here we show the results of a simple doublet lens that was assembled using all off-the-shelf optics that improves the resolution of our mid-IR microscope by reducing the chromatic aberration present in the system. While our design does not address as wide a wavelength range nor diminish the chromatic aberration as much as some alternative solutions, it is intended to work as a cost- and time- effective solution for ultrafast mid-IR hyperspectral imaging in the 4-6 μ m (\sim 1665-2500 cm $^{-1}$) range, for both optical (intensity) and chemical absorption imaging. We also hope to further explore the use of the doublet lens with microspheres, and test different materials to compare how they interact with the combination of materials present in the doublet lens.

- **Funding.** This work was funded under NSF 2108727
- **Acknowledgments.** We would like to thank Dean Edun for valuable discussions.
- **Disclosures.** The authors declare no conflicts of interest.
- **Data availability.** Data underlying the results presented in this paper are not publicly available at this time but may be obtained from the authors upon reasonable request.
- 360 Supplemental document.

363 References

365 Click or tap here to enter text.

367 368 369 370	1.	S. Veerasingam, M. Ranjani, R. Venkatachalapathy, A. Bagaev, V. Mukhanov, D. Litvinyuk, M. Mugilarasan, K. Gurumoorthi, L. Guganathan, V. M. Aboobacker, and P. Vethamony, "Contributions of Fourier transform infrared spectroscopy in microplastic pollution research: A review," Crit Rev Environ Sci Technol 51 , 2681–2743 (2021).
371 372	2.	Y. Bai, D. Zhang, L. Lan, Y. Huang, K. Maize, A. Shakouri, and J. X. Cheng, "Ultrafast chemical imaging by widefield photothermal sensing of infrared absorption," Sci Adv 5 , (2019).
373 374 375	3.	F. Rosi, C. Miliani, R. Braun, R. Harig, D. Sali, B. G. Brunetti, and A. Sgamellotti, "Noninvasive Analysis of Paintings by Mid-infrared Hyperspectral Imaging," Angewandte Chemie International Edition 52 , 5258–5261 (2013).
376 377 378	4.	B. Das, S. Roychowdhury, P. Mohanty, A. Rizuan, J. Chakraborty, J. Mittal, and K. Chattopadhyay, "A Zndependent structural transition of SOD1 modulates its ability to undergo phase separation," EMBO J 42 , e111185 (2023).
379 380	5.	D. N. Edun, M. R. Flanagan, and A. L. Serrano, "Does liquid-liquid phase separation drive peptide folding?," Chem Sci 12 , 2474–2479 (2021).
381 382	6.	A. Ghosh, J. S. Ostrander, and M. T. Zanni, "Watching Proteins Wiggle: Mapping Structures with Two-Dimensional Infrared Spectroscopy," Chem Rev 117 , 10726–10759 (2017).
383 384	7.	A. Ebner, P. Gattinger, I. Zorin, L. Krainer, C. Rankl, and M. Brandstetter, "Diffraction-limited hyperspectral mid-infrared single-pixel microscopy," Sci Rep 13 , 281 (2023).
385 386	8.	M. Jackson, M. G. Sowa, and H. H. Mantsch, "Infrared spectroscopy: A new frontier in medicine," in <i>Biophysical Chemistry</i> (Elsevier B.V., 1997), Vol. 68, pp. 109–125.
387 388 389	9.	P. Lasch, M. Stämmler, M. Zhang, M. Baranska, A. Bosch, and K. Majzner, "FT-IR Hyperspectral Imaging and Artificial Neural Network Analysis for Identification of Pathogenic Bacteria," Anal Chem 90 , 8896–8904 (2018).
390 391 392	10.	M. Hermes, R. B. Morrish, L. Huot, L. Meng, S. Junaid, J. Tomko, G. R. Lloyd, W. T. Masselink, P. Tidemand-Lichtenberg, C. Pedersen, F. Palombo, and N. Stone, "Mid-IR hyperspectral imaging for label-free histopathology and cytology," Journal of Optics (United Kingdom) 20 , 023002 (2018).
393 394	11.	R. A. Schultz, T. Nielsen, J. R. Zavaleta, R. Ruch, R. Wyatt, and H. R. Garner, "Hyperspectral imaging: A novel approach for microscopic analysis," Cytometry 43 , 239–247 (2001).
395 396	12.	K. Ataka, S. T. Stripp, and J. Heberle, "Surface-enhanced infrared absorption spectroscopy (SEIRAS) to probe monolayers of membrane proteins," Biochim Biophys Acta Biomembr 1828 , 2283–2293 (2013).
397 398	13.	A. L. Serrano, A. Ghosh, J. S. Ostrander, and M. T. Zanni, "Wide-field FTIR microscopy using mid-IR pulse shaping," Opt Express 23 , 17815 (2015).
399	14.	C. R. Baiz, D. Schach, and A. Tokmakoff, "Ultrafast 2D IR microscopy," Opt Express 22, 18724 (2014).
400 401	15.	S. Junaid, J. Tomko, M. P. Semtsiv, J. Kischkat, W. T. Masselink, C. Pedersen, and P. Tidemand-Lichtenberg, "Mid-infrared upconversion based hyperspectral imaging," Opt Express 26 , 2203 (2018).
402 403 404	16.	C. A. Tibbetts, A. B. Wyatt, B. M. Luther, and A. T. Krummel, "Practical Aspects of 2D IR Microscopy," in <i>Emerging Trends in Chemical Applications of Lasers</i> (American Chemical Society, 2021), Vol. 1398, pp. 109–134.

405 406	17.	J. S. Ostrander, A. L. Serrano, A. Ghosh, and M. T. Zanni, "Spatially Resolved Two-Dimensional Infrared Spectroscopy via Wide-Field Microscopy," ACS Photonics 3 , 1315–1323 (2016).
407 408	18.	A. Dorsa, Q. Xie, M. Wagner, and X. G. Xu, "Lock-in amplifier based peak force infrared microscopy," Analyst 148 , 227–232 (2023).
409 410	19.	G. Srinivasan and R. Bhargava, "Fourier transform-infrared spectroscopic imaging: The emerging evolution from a microscopy tool to a cancer imaging modality," Spectroscopy (Santa Monica) 22 , 30–43 (2007).
411 412 413	20.	B. Holcombe, A. Foes, S. Banerjee, K. Yeh, SH. J. Wang, R. Bhargava, and A. Ghosh, "Intermediate antiparallel beta structure in amyloid plaques revealed by infrared spectroscopic imaging," bioRxiv 2023.04.18.537414 (2023).
414 415	21.	B. J. Davis, P. S. Carney, and R. Bhargava, "Theory of mid-infrared absorption microspectroscopy: II. Heterogeneous samples," Anal Chem 82 , 3487–3499 (2010).
416 417 418	22.	N. Kröger, A. Egl, M. Engel, N. Gretz, K. Haase, I. Herpich, B. Kränzlin, S. Neudecker, A. Pucci, A. Schönhals, J. Vogt, and W. Petrich, "Quantum cascade laser–based hyperspectral imaging of biological tissue," J. Biomed. Opt 19 , 111607 (2014).
419 420 421	23.	E. N. Lewis, I. W. Levin, P. J. Treado, R. C. Reeder, G. M. Story, A. E. Dowrey, and C. Marcott, "Fourier Transform Spectroscopic Imaging Using an Infrared Focal-Plane Array Detector," Anal Chem 67 , 3377–3381 (1995).
422 423 424	24.	F. S. Ruggeri, J. Habchi, S. Chia, R. I. Horne, M. Vendruscolo, and T. P. J. Knowles, "Infrared nanospectroscopy reveals the molecular interaction fingerprint of an aggregation inhibitor with single Aβ42 oligomers," Nat Commun 12 , (2021).
425 426	25.	K. L. A. Chan and S. G. Kazarian, "Correcting the effect of refraction and dispersion of light in FT-IR spectroscopic imaging in transmission through thick infrared windows," Anal Chem 85 , 1029–1036 (2013).
427 428	26.	G. E. Greaves, D. Kiryushko, H. W. Auner, A. E. Porter, and C. C. Phillips, "Label-free nanoscale mapping of intracellular organelle chemistry," Commun. Biol 6 , 583 (2023).
429 430	27.	D. Bracha, M. T. Walls, and C. P. Brangwynne, "Probing and engineering liquid-phase organelles," Nat Biotechnol 37 , 1435–1445 (2019).
431 432	28.	H. Zhang, S. Shao, Y. Sun, H. Zhang, S. Shao, and Y. Sun, "Characterization of liquid–liquid phase separation using super-resolution and single-molecule imaging," Biophys Rep 8 (1), 2–13 (2022).
433 434	29.	X. Zhang, H. Li, Y. Ma, D. Zhong, and S. Hou, "Study liquid-liquid phase separation with optical microscopy: A methodology review," APL Bioeng 7 , 21502 (2023).
435 436 437	30.	K. Tachi, T. Hirasawa, S. Okawa, A. Horiguchi, K. Ito, and M. Ishihara, "Chromatic-aberration-free multispectral optical-resolution photoacoustic microscopy using reflective optics and a supercontinuum light source," Appl Opt 60 , 9651 (2021).
438 439	31.	P. Wang, N. Mohammad, and R. Menon, "Chromatic-aberration-corrected diffractive lenses for ultra-broadband focusing," Sci Rep 6 , 1–7 (2016).
440 441	32.	B. Guo, Y. Wang, C. Peng, H. L. Zhang, G. P. Luo, H. Q. Le, C. Gmachl, D. L. Sivco, M. L. Peabody, and A. Y. Cho, "Laser-based mid-infrared reflectance imaging of biological tissues," Opt Express 12 , (2004).
442 443	33.	J. Kilgus, G. Langer, K. Duswald, R. Zimmerleiter, I. Zorin, T. Berer, and M. Brandstetter, "Diffraction limited mid-infrared reflectance microspectroscopy with a supercontinuum laser," Opt Express 26 , (2018).

444 445	34.	J. Sasian, "Method to design apochromat and superachromat objectives," Optical Engineering 56 , 1 (2017).
446 447	35.	Q. Lu, Y. Ding, W. Wang, S. Liu, and M. Xu, "VIS-NIR superachromatic triplet design with five-color correction for a broadband interferometer," Appl Opt 61 , 8880 (2022).
448 449	36.	A. M. Hanninen and E. O. Potma, "Nonlinear optical microscopy with achromatic lenses extending from the visible to the mid-infrared," APL Photonics 4 , 080801 (2019).
450	37.	A. P. Wood, "Design of infrared hybrid refractive–diffractive lenses," Appl Opt 31 , 2253 (1992).
451 452	38.	Y. Qiu, J. Li, T. Li, X. Ma, and X. Jiang, "Photo-Curing Vis-IR Hybrid Fresnel Lenses with High Refractive Index," Macromol Chem Phys 222 , 2100311 (2021).
453 454	39.	Y. Yuan, Z. Yan, P. Zhang, Z. Chang, F. Peng, R. Chen, Z. Yang, S. Chen, Q. Zhao, and X. Huang, "A Broadband Achromatic Dielectric Planar Metalens in Mid-IR Range," Photonic Sensors 13 , 1–9 (2023).
455 456	40.	F. Aieta, M. A. Kats, P. Genevet, and F. Capasso, "Multiwavelength achromatic metasurfaces by dispersive phase compensation," Science (1979) 347 , 1342–1345 (2015).
457	41.	N. Ji, "Adaptive optical fluorescence microscopy," Nat Methods 14, 374–380 (2017).
458	42.	P. S. Salter and M. J. Booth, "Adaptive optics in laser processing," Light Sci Appl 8, 1–16 (2019).
459 460	43.	Y. Liu, ZH. Yang, YJ. Yu, LA. Wu, MY. Song, and ZH. Zhao, "Chromatic-Aberration-Corrected Hyperspectral Single-Pixel Imaging," Photonics 10 , 7 (2022).
461 462	44.	J. Wu, D. Li, A. Cui, J. Gao, K. Zhou, and B. Liu, "Digital infrared chromatic aberration correction algorithm for membrane diffractive lens based on coherent imaging," Appl Opt 61 (34), 10080–10085 (2022).
463 464	45.	J. T. Korneliussen and K. Hirakawa, "Camera processing with chromatic aberration," IEEE Transactions on Image Processing 23 , 4539–4552 (2014).
465 466	46.	M. Kozubek and P. Matula, "An efficient algorithm for measurement and correction of chromatic aberrations in fluorescence microscopy," J Microsc 200 , 206–217 (2000).
467 468	47.	M. M. Eid, "Characterization of Nanoparticles by FTIR and FTIR-Microscopy," Handbook of Consumer Nanoproducts 1–30 (2021).
469 470	48.	G. L. Liu and S. G. Kazarian, "Recent advances and applications to cultural heritage using ATR-FTIR spectroscopy and ATR-FTIR spectroscopic imaging," Analyst 147 , 1777–1797 (2022).
471 472	49.	K. Seidl, J. Knobbe, and H. Grüger, "Design of an all-reflective unobscured optical-power zoom objective," Appl. Opt. 48 (21), 4097-4107 (2009).
473 474 475 476	50.	K. Yeh, I. Sharma, K. Falahkheirkhah, M. P. Confer, A. C. Orr, Y. T. Liu, Y. Phal, R. J. Ho, M. Mehta, A. Bhargava, W. Mei, G. Cheng, J. C. Cheville, and R. Bhargava, "Infrared spectroscopic laser scanning confocal microscopy for whole-slide chemical imaging," Nature Communications 2023 14:1 14 , 1–12 (2023).
477 478 479	51.	E. S. Lee, SW. Lee, J. Hsu, E. O. Potma, H. 3 R. C. Mendelsohn, M. E. Chen, and D. J. Rerek, "Vibrationally resonant sum-frequency generation microscopy with a solid immersion lens," Biomed. Opt. Express 5 (7), 2125-2134 (2014).

480 481	52.	K. L. A. Chan and S. G. Kazarian, "Aberration-free FTIR spectroscopic imaging of live cells in microfluidic devices," Analyst 138 , 4040–4047 (2013).
482 483 484 485	53.	K. L. A. Chan, A. Altharawi, P. Fale, C. L. Song, S. G. Kazarian, G. Cinque, V. Untereiner, and G. D. Sockalingum, "Transmission Fourier Transform Infrared Spectroscopic Imaging, Mapping, and Synchrotron Scanning Microscopy with Zinc Sulfide Hemispheres on Living Mammalian Cells at Sub-Cellular Resolution," Appl Spectrosc 74 , 544–552 (2020).
486 487	54.	J. A. Kimber, L. Foreman, B. Turner, P. Rich, and S. G. Kazarian, "FTIR spectroscopic imaging and mapping with correcting lenses for studies of biological cells and tissues," Faraday Discuss 187 , 69–85 (2016).
488 489	55.	X. Hao, C. Kuang, X. Liu, H. Zhang, and Y. Li, "Microsphere based microscope with optical super-resolution capability," Appl Phys Lett 99 , 203102 (2011).
490 491 492	56.	K. W. Allen, N. Farahi, Y. Li, N. I. Limberopoulos, D. E. Walker, A. M. Urbas, V. Liberman, and V. N. Astratov, "Super-resolution microscopy by movable thin-films with embedded microspheres: Resolution analysis," Ann Phys 527 , 513–522 (2015).
493 494	57.	H. Yang, N. Moullan, J. Auwerx, and M. A. M. Gijs, "Super-Resolution Biological Microscopy Using Virtual Imaging by a Microsphere Nanoscope," Small 10 , 1712–1718 (2014).
495 496 497 498	58.	V. N. Astratov, A. V. Maslov, K. W. Allen, N. Farahi, Y. Li, A. Brettin, N. I. Limberopoulos, D. E. Walker, A. M. Urbas, V. Liberman, and M. Rothschild, "Fundamental limits of super-resolution microscopy by dielectric microspheres and microfibers," in <i>Nanoscale Imaging, Sensing, and Actuation for Biomedical Applications XIII</i> (SPIE) (2016), paper 97210K.
499 500 501	59.	D. N. Edun, C. E. Nelmark, and A. L. Serrano, "Resolution Enhancement in Wide-Field IR Imaging and Time-Domain Spectroscopy Using Dielectric Microspheres," Journal of Physical Chemistry A 124 , 5534–5541 (2020).
502 503	60.	B. S. Luk'yanchuk, R. Paniagua-Domínguez, I. Minin, O. Minin, and Z. Wang, "Refractive index less than two: photonic nanojets yesterday, today and tomorrow [Invited]," Opt Mater Express 7 , 1820 (2017).
504 505	61.	H. Yang, R. Trouillon, G. Huszka, and M. A. M. Gijs, "Super-Resolution Imaging of a Dielectric Microsphere Is Governed by the Waist of Its Photonic Nanojet," Nano Lett 16 , 4862–4870 (2016).
506 507	62.	J. Liang, M. Tu, W. Liu, Z. Qiao, G. Cui, al Jianfeng Liang, and W. Peng, "Optical constant determination of cross-linked polystyrene in the infrared," 10623 , 63–68 (2018).
508 509 510	63.	B. Boeckx, R. Ramaekers, and G. Maes, "The influence of the peptide bond on the conformation of amino acids: A theoretical and FT-IR matrix-isolation study of N-acetylproline," Biophys Chem 159 , 247–256 (2011).
511 512	64.	Z. Zhang and R. Lu, "Initial structure of dispersion objective for chromatic confocal sensor based on doublet lens," Opt Lasers Eng 139 , 106424 (2021).
513	65.	B. Gleason, "Designing Optical Properties in Infrared Glass," Ph.D. dissertation (Clemson University, 2015).
514	66.	Zemax (An Ansys Company); OpticStudio.
515 516	67.	A. R. Salvà, "OUFTI-NEXT: STUDY OF REFRACTIVE LENSES FOR AN INFRARED CAMERA," Master's Thesis (The Technical University of Catalonia, 2019).
517 518	68.	K. Yeh, S. Kenkel, J. N. Liu, and R. Bhargava, "Fast infrared chemical imaging with a quantum cascade laser," Anal Chem 87 , 485–493 (2015).68. S. Ran, S. Berisha, R. Mankar, WC. Shih, and D. Mayerich,

519 520		"Mitigating fringing in discrete frequency infrared imaging using time-delayed integration," Biomed Opt Express 9 , 832 (2018).
521 522	69.	S. Ran, S. Berisha, R. Mankar, WC. Shih, and D. Mayerich, "Mitigating fringing in discrete frequency infrared imaging using time-delayed integration," Biomed Opt Express 9 , 832 (2018).
523		
524		
525		
526		